ACKNOWLEDGMENT

The authors would like to thank Prof. J. Zhang and J. Li, Dr. B. Zhen and S. Zhao for their help during IVUS experiment.

REFERENCES

[1] R. Myler and S. Stertzer, *Coronary and Peripheral Angioplasty: Historic Perspective, Textbook of Interventional Cardiology*, 2nd ed, E. Topol, Ed. Philadelphia, PA: Saunders, 1993, vol. 1.

[2] C. L. De Korte, E. I. Cespedes, and C. T. Lancee, "Intravascular elasticity imaging using ultrasound: Feasibility studies in phantoms," *Ultrasound Med. Biol.*, vol. 23, no. 5, pp. 735–746, 1997.

[3] B. M. Shapo, J. R. Crowe, A. R. Skovoroda, M. J. Eberle, N. A. Cohn, and M. O'Donnell, "Displacement and strain imaging of coronary arteries with intravascular ultrasound," *IEEE Trans. Ultrason. Ferroelect. Freq. Contr.*, vol. 43, pp. 234–246, Mar. 1996.

[4] H. E. Talhami, L. S. Wilson, and M. L. Neale, "Spectral tissue strain: A new technique for imaging tissue strain using intravascular ultrasound," *Ultrasound Med. Biol.*, vol. 20, no. 8, pp. 759–772, 1994.

[5] L. K. Ryan and F. S. Foster, "Ultrasonic measurement of differential displacement and strain in a vascular model," *Ultrason. Imag.*, vol. 19, pp. 19–38, 1997.

[6] G. Finet, E. Maurincomme, A. Tabib, R. J. Crowley, I. Magnin, R. Roriz, J. Beaune, and M. Amiel, "Artifacts in intravascular ultrasound imaging: Analyzes and implications," *Ultrasound Med. Biol.*, vol. 19, no. 7, pp. 533–547, 1993.

[7] P. P. Kearney and M. P. Ramo, "A study of the quantitative and qualitative impact of catheter shaft angulation in a mechanical intravascular ultrasound system," *Ultrasound Med. Biol.*, vol. 23, no. 1, pp. 87–93, 1997.

[8] M. X. Wan, Y. M. Li, J. B. Li, and Y. Y. Cui, "Elasticity imaging of artery walls with intravascular ultrasound," in *Proc. 20th Annu. Int. Conf. IEEE-EMBS*, Hongkong, 1998, pp. 860–861.

[9] B. K. P. Horn and B. G. Schunck, "Determining optical flow," *Artif. Intell.*, vol. 17, no. 1, pp. 185–203, Aug. 1981.

[10] A. Giachetti and V. Torre, "The use of optical flow for the analysis of nonrigid motion," *Int. J. Comput. Vis.*, vol. 18, no. 3, pp. 255–279, 1996.

[11] E. De Micheli, V. Torre, and S. Uras, "The accuracy of the computation of optical flow and of the recovery of motion parameters," *IEEE Trans. Pattern Anal. Machine Intell.*, vol. 15, pp. 434–447, May 1993.

[12] G. L. Chen, X. F. Wang, Z. Q. Zhuang, and D. S. Wang, *Theory and Application of Genetic Algorithms*. Beijing, China: People's Posts & Telecommunications, 1996.

[13] A. R. Skovoroda, S. Y. Emelianov, and M. O'Donnell, "Tissue elasticity reconstruction based on ultrasonic displacement and strain images," *IEEE Trans. Ultrason. Ferroelect. Freq. Contr.*, vol. 42, pp. 747–765, July 1995.

[14] M. A. Lubinski and S. Y. Emelianov, "Lateral displacement estimation using tissue incompressibility," *IEEE Trans. Ultrason. Ferroelect. Freq. Contr.*, vol. 43, pp. 247–255, Mar. 1996.

[15] F. Kallel and M. Bertrand, "Tissue elasticity reconstruction using linear perturbation method," *IEEE Trans. Med. Imag.*, vol. 15, pp. 299–313, June 1996.

[16] G. E. Maillous, F. Langlois, P. Y. Simard, and M. Bertrand, "Restoration of the velocity field of the heart from two-dimensional echocardiograms," *IEEE Trans. Med. Imag.*, vol. 8, pp. 143–153, June 1989.

Toward a Better Understanding of Texture in Vascular CT Scan Simulated Images

J. Bézy-Wendling*, M. Kretowski, Y. Rolland, and W. Le Bidon

***Abstract*—This paper shows the influence of computed tomography slice thickness on textural parameters by simulating realistic images issued from: 1) a 3D model of vascular tree, with structural and functional features and in which angiogenesis is related to the organ growth; 2) a projection/reconstruction process using fast Fourier transform. Texture analysis is performed by means of second-order statistics and gradient based methods.**

***Index Terms*—Image analysis, texture simulation, vascular modeling.**

I. INTRODUCTION

Texture analysis is an efficient tool to characterize normal and diseased living tissues [1]. However, textural features are strongly influenced by the image acquisition conditions. Modeling the tissue and the image generation is a very good mean of studying these variations, as far as sound physiologically based objects and physically based imaging are both used.

The three-dimensional (3-D) objects we use for image simulation are vascular trees (Fig. 1). Indeed, in many cases, vessels are important primitives in medical images, when enhanced by a contrast product. Blood vessels are good markers of pathophysiological modifications of tissues: their structure, density, and geometry are often changed when a disease appears and develops. Such models have been reported before. Gottlieb [2] proposed a two-dimensional (2-D) model where the growth of the tree depends on the organ development, but hemodynamic behavior of blood is not simulated. The model of Schreiner [3] is more complete: geometrical and functional properties of the tree are well simulated, but it is still a 2-D model and it does not allow to simulate pathological cases. More recently, a 3-D extension of this work has been proposed [4]. Our model [5], [6] is a functional 3-D one. Moreover, vascular modifications due to pathology (changes of vascular density, pressure, blood flow) can easily be simulated. The main concepts of the model presented in [5], [6] are close to those reported in [4]. The vessels (rigid tubes forming a binary tree) grow to irrigate macro-cells uniformly distributed in a 3-D organ (static shape in [4], growing in [5] and [6]). In both cases, blood is considered as a Newtonian fluid whose flow is governed by Poiseuille's law. Similarly, two optimization levels are distinguished: a geometrical optimization of the new bifurcation (minimizing the volume of blood added), and a more global process consisting in re-computing

Manuscript received May 29, 2000; revised September 21, 2000. *Asterisk indicates corresponding author*.

*J. Bézy-Wendling is with the Laboratoire Traitement du Signal et de l'Image, INSERM, Université de Rennes 1, Bâtiment 22, Campus de Beaulieu, 35042 Rennes Cedex, France (e-mail: johanne.bezy@univ-rennes1.fr).

M. Kretowski is with the Laboratoire Traitement du Signal et de l'Image, INSERM, Université de Rennes 1, Campus de Beaulieu, 35042 Rennes Cedex, France. He is also with the Institute of Computer Science, Technical University of Bialystok, 15-405 Bialystok, Poland.

Y. Rolland is with the Laboratoire Traitement du Signal et de l'Image, INSERM, Université de Rennes 1, Campus de Beaulieu, 35042 Rennes Cedex, France. He is also with the Département de Radiologie et d'Imagerie Médicale (DRIMS), CHR Hôpital Sud, 35000 Rennes, France.

W. Le Bidon are with the Laboratoire Traitement du Signal et de l'Image, INSERM, Université de Rennes 1, Campus de Beaulieu, 35042 Rennes Cedex, France.

Publisher Item Identifier S 0018-9294(01)00144-6.

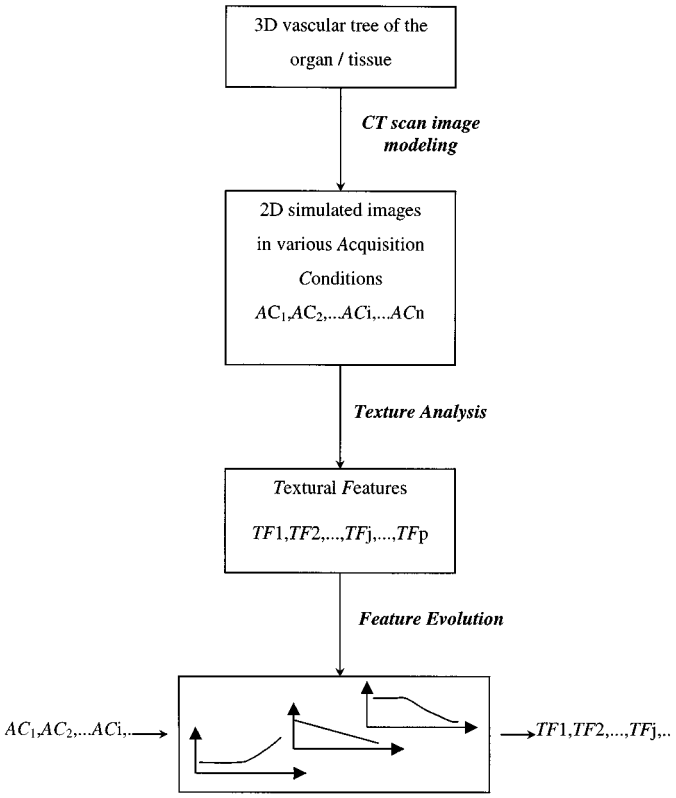

Fig. 1. A framework to better understand textural feature variations. Simulation of 3-D vascular trees is followed by simulation of CT images. The influence of the vascular parameters and of the acquisition conditions on textural features is studied.

(in slightly different ways) radii of the tree after addition of a new cell. The advances presented in [4] deal with the extension of the 2-D model first presented in [3], and the introduction of terminal flow variability, which influences the structure and the geometry of the vascular tree. This property could be compared to the one we used in [5], [6], where several classes of cells, with different geometrical and physiological properties coexist in a same organ, leading to various kinds of vascular regions (hyper-vascularized/normal for example).

In a previous study [7], CT scan acquisitions have been simulated using a simplified method and the capability of textural features in discriminating between normal and hyper vascularization situations has been examined. In this paper, we present a more realistic method of CT scan image generation by fully representing the interactions between X-rays and tissues. In Section II, the model used to create 3-D vascular trees is briefly presented. In Section III, the projection and backprojection process is described and results of texture analysis are given and discussed in Section IV.

II. Three-Dimensional Vascular Tree Modeling

The tissue is made of units (macrocells), characterized by geometric and hemodynamic properties (refer for more details to [5] and [6]). The parameters of a macrocell are its size, the radius of its irrigating vessel (which corresponds to the smallest modeled vessel) and its class (normal or pathological, with several possible pathologies). A maximum density (number of macrocells in a given tissue region) and a subdivision time rate are associated with each class of cells. The birth of a new cell gives rise to the birth of a small vessel, which will grow in order to irrigate the cell.

TABLE I
Parameters Used to Simulate the 3-D Hepatic Arterial Tree

Adult liver size (cm^3)	1500
Hepatic artery blood flow (ml/min)	400
Hepatic artery blood pressure (mm Hg)	98
Size of the « macrocell » (cm^3)	0.125
Number of macrocells in the adult organ	12000
Macrocell blood consumption (ml/min)	0.033
Radius of the smallest vessel irrigating the macrocell (mm)	0.1

Two optimization processes are used during the growth of the tree. When a small vessel is created, the new bifurcation is locally optimized (we chose the minimum blood volume as the target function). A global optimization procedure is also used to guarantee, at every stage of the growth, that a geometric relation between radii in each bifurcation ($R^\gamma = R^\gamma_{\text{left}} + R^\gamma_{\text{right}}$) and hemodynamic (blood pressure at the tree input and at its extremities, blood flow) constraints are satisfied. The main physical laws used in the optimization steps are Poiseuille's law and the matter conservation property (blood flow in a father vessel is equal to the sum of blood flows in its two children).

The 3-D model used in this paper simulates the hepatic arterial tree (Table I). The liver was made of two classes of macrocells: normal and pathological. The latter cells needs more blood, divide more quickly and their maximum density is higher than that of normal macrocells. A hyper-vascularized region can then be generated in the vascular tree (Fig. 2).

III. CT Scan Image Simulation

The geometrically based method reported in [7] consisted to look for the intersection between each vessel of the vascular tree and the given slice plane with a known thickness. Vessels whose diameters were greater than the pixel size appeared clearly like spots with shapes and intensities depending on the vessels caliber and orientation with respect to the slice, and the slice thickness. Here, a full projection-backprojection process is applied.

The first step consists to create of a 3-D map (i.e., 256^3) in which each voxel is characterized by a density, taking into account the partial volume effect. The density of a voxel intersecting partially a vessel is proportional to the volume of the voxel filled by blood. Its value is computed according to control points regularly distributed into the voxel (Fig. 3) and situated inside the vessel. The number of control points influences the number of vessels effectively represented in the 3-D map (here we used 5^3 points, which provides a more precise image than 3^3). The densities of a voxel included in a vessel or only made of parenchyma have been respectively set to 220 and 70 (classical values of density for respectively the blood, and the noninjected liver). A gaussian noise has been added to the parenchyma in order to render the spatial variations of microvessels. Its standard deviation (σ) can vary according to the class of tissue. The values we chose ($\sigma = 10$ for normal, $\sigma = 20$ for hyper vascularized) have been *a priori* determined. Measures made on real images should give us more precise values.

Using this data volume, the CT scan acquisition is carried out in two steps: X-ray projections are computed, using the Radon function

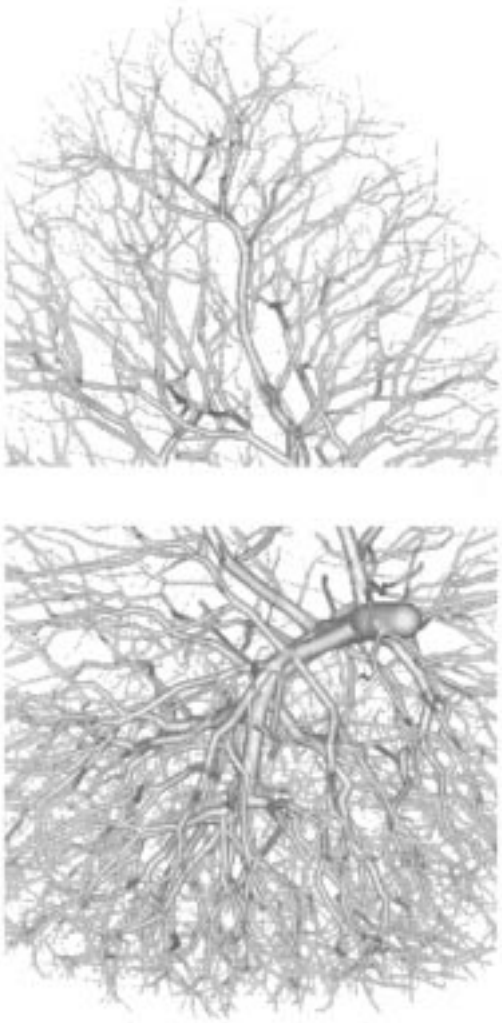

Fig. 2. Vascular tree simulated with parameters of Table I. Two regions with different vascular properties can be distinguished: a normally vascularized region (top) and a hyper-vascularized region (bottom).

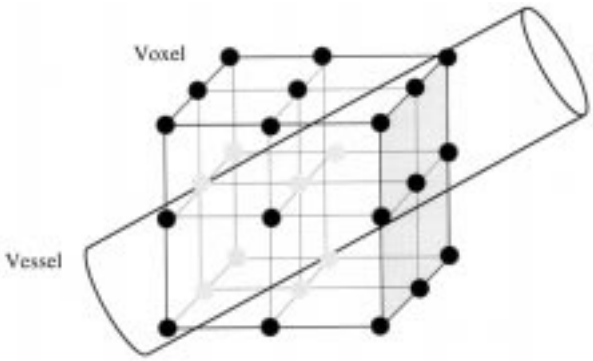

Fig. 3. The density assigned to a voxel is proportional to the volume of the voxel inside a vessel. To compute it, control points distributed in the voxel are used.

and, the filter back-projection method [8], [9] is used to reconstruct the image.

In order to take into account the thickness of the beam, not only the voxel intersected by a ray has to be considered but also its neighbors, that have also been touched by the beam. An interpolation method is applied to compute the resulting attenuation (the contribution of a neighbor with density a and whose center is situated at a distance D of the point is set to $a(1-D)$). Then the sum, for each ray, of the attenuation values for all the voxels situated on the ray, provides the projection map.

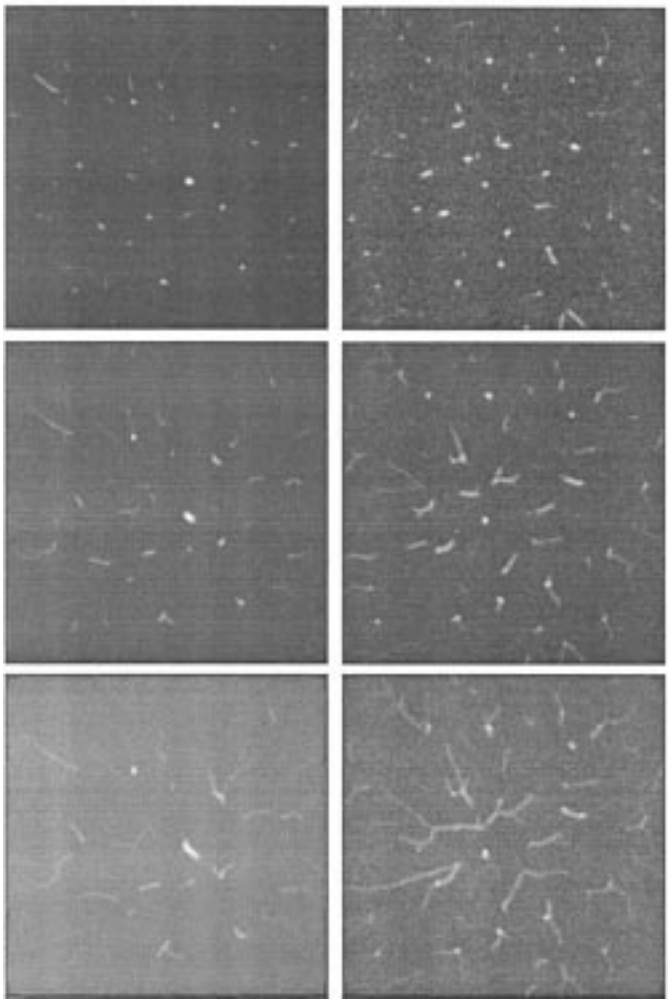

Fig. 4. Six examples of CT scan simulated images, from the tree of Fig. 2. Left: Images simulated in the normally vascularized region, with 1-mm (top), 4-mm (middle) and 8-mm (bottom) slice thickness. The standard deviation of the gaussian noise used to simulate parenchyma is $\sigma = 10$. Right: Corresponding images simulated in the hyper vascularized region of the tree, with $\sigma = 20$.

For each projection angle, the projections are filtered before proceeding to the back-projection. A fast Fourier transform (FFT) algorithm is used to obtain the Fourier coefficients $F(\omega)$. These coefficients are then multiplied by $|\omega|$ before coming back to the spatial domain by an inverse FFT.

This approach allows modifying the image resolution as well as the slice thickness. The resolution is set during the density map generation. To increase or decrease the resolution, a zoom factor can be applied to a 3-D region of interest in the tree. The slice thickness is taken into account during the projection step. To compute the projection value along a given direction, the attenuation coefficients of the voxels belonging to a number of layers (with constant thickness of 0.25 mm), depending of the desired thickness, are summed.

IV. Results and Discussion

Slice images were generated from the hepatic arterial tree with a thickness ranging from 1 mm to 8 mm (Fig. 4) and for normal and

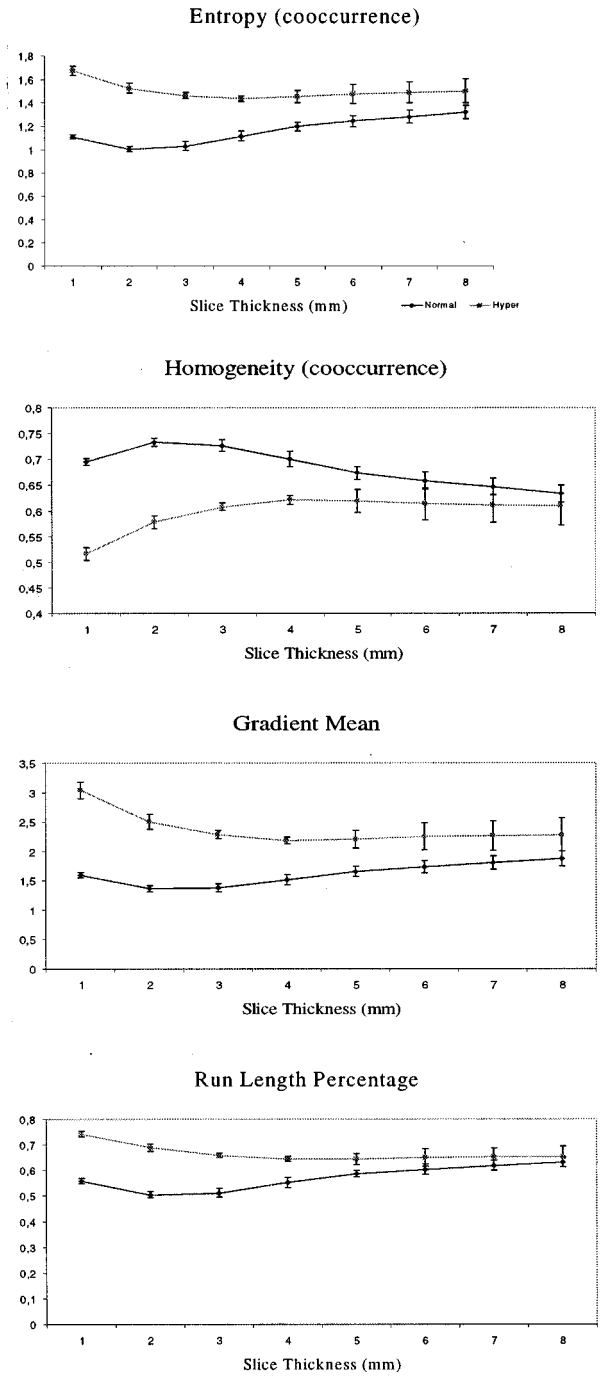

Fig. 5. Evolution of some textural features (vertical orientation) according to the slice thickness (standard deviation are represented by vertical bars).

hyper-vascularized regions of the organ displayed Fig. 2 (the spatial resolution is 0.25 mm).

They show that vessel patterns go from spot-like to ribbon-like shapes when the slice thickness is increased. A clear differentiation can be visually done between normal and hyper vascularized tissues. The smoothing due to the projection/back-projection procedure leads to less contrasted images when compared to the results previously published on simulated data but more similar to real images [7]. A quantitative analysis has been performed. Most of the textural features available from the literature have been computed (theoretical formulations can be found in [1]). Only some of them are displayed Fig. 5, as a function of slice thickness for two types of vascularization (normal and hyper). The parameter values have been computed on 12 regions of interest (ROIs) (four per image and three images corresponding to different anatomical positions in the organ). The vertical bars represent standard deviations. The influence of the number of ROIs on the results has not been precisely studied at the moment.

These results confirm the capability to discriminate normal vascularization and hyper vascularization situations as described in our first study [7]. They also point out that the relative values characterizing normal vascularization and hyper vascularization are preserved for each of these four features.

However, it has to be noticed that evolution of textural features is not exactly the same with the two methods of image generation. For example, looking at the "homogeneity" graphs, it can be seen that, with the first method, this feature decreased with the slice thickness, while with the second method, it slightly increases before decreasing or becoming stable. Both kinds of variation can be explained. In images computed in our previous work, both micro- and macro-texture are less homogeneous when slice thickness increases. In the present case, we first studied texture given by vessels solely, and in a second time, texture corresponding to parenchyma exclusively. The "homogeneity" feature computed on vessels only is relatively stable with thickness less than 4 mm, and then decreases. Conversely, for tissue only, the homogeneity progressively increases with thickness. It appears that the global evolution of "homogeneity" with the slice thickness is the result of a combination between these two processes: when the slice thickness is lower than 4 mm, parenchyma is most prominent while, when the slice thickness is higher than 4 mm, the vessels, which are more and more visible, have more importance than parenchyma.

The evolution of the three other features can be explained in the same way: the contribution of each component to the textural mixture can vary in different ways and it is of critical importance to set the acquisition conditions accordingly.

V. Conclusion

It has been shown that simulation can help for better designing imaging protocols in order to objectively characterize and differentiate tissue patterns. A systematic examination of all the factors influencing and contributing to the final decision, from the living tissue modeling, to the image formation and to the texture analysis algorithms, is required. Then a real, physically based, understanding of textural features can be expected.

Acknowledgment

The authors are indebted to Prof. J. L. Coatrieux for his valuable contributions and encouragement.

References

[1] A. Bruno, R. Collorec, J. Bézy-Wendling, P. Reuzé, and Y. Rolland, "Texture analysis in medical imaging," in *3-D Biomedical Imaging*, C. Roux and J. L. Coatrieux, Eds: IOS, 1997, pp. 133–164.

[2] M. E. Gottlieb, "Modeling blood vessels: A deterministic method with fractal structure based on physiological rules," in *Proc. Int. Conf. IEEE Engineering in Medicine and Biology Society*, vol. 12, 1990.

[3] W. Schreiner and P. Buxbaum, "Computer optimization of vascular trees," *IEEE Trans. Biomed. Eng.*, vol. 40, May 1993.

[4] R. Karch, F. Neumann, M. Neumann, and W. Schreiner, "A three-dimensional model for arterial tree representation, generated by constrained constructive optimization," *Comput. Biol. Med.*, vol. 29, no. 1, pp. 19–38, 1999.

[5] J. Bézy-Wendling and A. Bruno, "A 3-D dynamic model of vascular trees," *J. Biol. Syst.*, vol. 7, no. 1, pp. 11–31, 1999.

[6] Y. Rolland, J. Bézy-Wendling, R. Duvauferrier, and A. Bruno, "Modeling of the parenchymous vascularization and perfusion," *Investigat. Radiol.*, vol. 34, no. 3, pp. 171–175, 1999.

[7] Y. Rolland, J. Bézy-Wendling, R. Duvauferrier, and J. L. Coatrieux, "Slice simulation from a model of the parenchymous vascularization to evaluate texture features," *Investigat. Radiol.*, vol. 34, no. 3, pp. 181–184, 1999.
[8] G. T. Herman, "Image reconstruction from projections—Three-dimensional biomedical imaging," presented at the 1st Int. Summer School of the IEEE Engineering in Medicine and Biology Society, Berder's Island, Brittany, France, July 2–10, 1994.
[9] A. K. Jain, *Fundamentals of Digital Image Processing*. Englewood Cliffs, NJ: Prentice-Hall, 1989.

The Case for Large-Size Mutations

Sid Deutsch

***Abstract*—There are no laws of physics or chemistry that forbid large mutations. Therefore, the "size" of a random mutation should fit the mathematics of a Poisson point process: The number of mutations (N), versus mutation size (MS), should obey an exponential relationship. Three examples are examined: A simple 15-mutation sequence; actual experimental data involving a sequence of 56 611 random action potentials (rather than mutations); and a synthetic sequence of 65 535 random mutations. In the latter example, with an average MS of 2.22 units, the largest MS is a 25-unit giant that would be associated with major changes.**

***Index Terms*—Evolution, living cell, mutation, Poisson point process, pseudorandom sequence.**

I. Introduction

In a recent special section on evolution, in *Science*, we find a statement such as [1] "...big, beneficial mutations were thought to come along so rarely that many models simply assumed that they play no part in adaptation. But as evolutionists begin to probe the genetic basis behind important adaptations, they are uncovering examples of such large mutations, dramatically revising how biologists think about evolutionary change." The purpose of the present paper is to show that "large-size" mutations are inevitable.

I am only discussing viable mutations, of course, the kind that each of us has survived despite 3.8 billion years of evolution, with an endless succession of mostly small, but occasionally large, mutational changes.

This is illustrated in Fig. 1, which depicts three short synthesized sections of a random sequence of 65 535 mutations. The "size" of each mutation is proportional to the interspike distance; this is probably the most meaningful and convenient way to convey the "size" of a mutation.

One can think of mutation size $= 1$ as representing a change in *one* nucleotide; for example, from thymine to guanine or vice versa. This depends, however, on the context: If the first living cell consists of a circular array of 100 atoms, say, then mutation size $= 1$ corresponds to a change in a single atom. (The present paper is restricted to conventional nucleotide mutations.)

Although Fig. 1 is based on a mathematical model, it will turn out that there is no escape from the conclusion that large-size mutations actually occur. It is not possible to only accept, as viable, tiny mutational changes. These are shown in Fig. 1(a), which summarizes the usual perception: Of the 26 randomly-occurring mutations shown, ten are minuscule [MS $= 1$]; six are of size $\mathrm{MS} = 2$; four of size $\mathrm{MS} = 3$; two each of $\mathrm{MS} = 4$ and $\mathrm{MS} = 5$; one of $\mathrm{MS} = 6$; and one "giant" of $\mathrm{MS} = 8$.

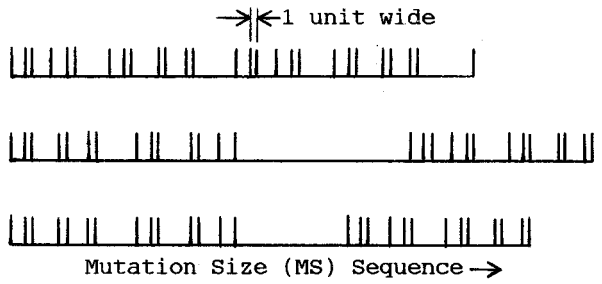

Fig. 1. Three short synthesized sections of a random sequence of 65 535 mutations. The *size* of each mutation corresponds to the distance between starting and ending spikes. (a) The usual perception that only small mutational changes are viable. The *average* mutation size (MS) is 2.5 units wide for the section shown. (b) The section that contains the largest mutation, a major change that is $\mathrm{MS} = 25$ units wide. The mutations before and after this giant are small, as in (a). (c) The section that contains a medium-large mutation, $\mathrm{MS} = 16$. Again, the mutations before and after are small, as in (a). [Because of the pseudorandom sequence used to synthesize the sections, (b) and (c) are almost identical.]

But consider another section of the 65 535-mutation sequence, that of Fig. 1(b). Here the largest mutation—with $\mathrm{MS} = 25$—is pictured near the center of the sequence. The $\mathrm{MS} = 25$ value is not a mathematical error; it is mathematically *certain* that huge mutations have to occur. Of course, any data that show up with such unexpected mutations would be, in many cases, discarded (the laboratory sheet would perhaps be torn up), hopefully accompanied by an explanation that the power failed, or a "bug" or gremlin momentarily took over. Outliers may sometimes be allowed; actually, in the present example, it could be more appropriate to discard Fig. 1(a) and retain Fig. 1(b).

II. An Inverse-Size Index

Let M represent an inverse-size index, so that $M = 1$ belongs to the widest mutation in the sequence, such as that near the center of Fig. 1(b). At the other extreme of M values, then, $M = 65\,535$ characterizes a mutation so small (calculation yields $\mathrm{MS} = 0.09$) that it is of negligible consequence. But examination of the full sequence would show that the gap of Fig. 1(b) is not alone. We have $M = 2$ ($\mathrm{MS} = 23$), M = 3 (MS = 22), and so forth. Fig. 1(c) depicts the sequence that contains $M = 63$, where the MS near the center has a medium-large value, 16.

If we plot the number of mutations of a particular size, N, versus the mutation size, MS, we get a straight line on a semi-log plot, as in Fig. 2(a). Obviously, entirely in agreement with the revelations of evolution, there is a large number of relatively small mutations and, of course, a small number of large mutations. Fig. 2 is a simple numerical example with a sequence of only 15 mutations, as shown in Fig. 2(b). (We will return to the 65 535-sequence example below.)

The straight line of Fig. 2(a) corresponds to a simple exponential equation

$$N = N_0 \varepsilon^{-\lambda \mathrm{MS}} \tag{1}$$

where N_0 is the zero-intercept value at MS= 0 [the line of Fig. 2(a) terminates at $N_0 = 7.5$]; λ is a slope coefficient [Fig. 2(a) is drawn with $\lambda = 0.45$].

Manuscript received March 3, 2000; revised September 19, 2000.
S. Deutsch, retired, 3967 Oakhurst Blvd., Sarasota, FL 34233 USA (e-mail: deutsch@eng.usf.edu).
Publisher Item Identifier S 0018-9294(01)00143-4.